Applied Catalysis B: Environmental 150–151 (2014) 656–662

Contents lists available at ScienceDirect

Applied Catalysis B: Environmental

journal homepage: www.elsevier.com/locate/apcatb

# Mesoporous Pt-$TiO_2$ thin films: Photocatalytic efficiency under UV and visible light

S. Semlali[a,b], T. Pigot[a,*], D. Flahaut[a], J. Allouche[a], S. Lacombe[a], L. Nicole[b]

[a] IPREM, UMR CNRS 5254, Université de Pau et des Pays de l'Adour, 25 Hélioparc, 2 rue du Président Angot, F-64053 Pau Cedex 9, France
[b] LCMCP, UMR CNRS 7574, Université Paris IV pierre et Marie Curie, Collège de France, 11 place Marcelin Berthelot, 75231 Paris, France

ARTICLE INFO

*Article history:*
Received 26 July 2013
Received in revised form
20 December 2013
Accepted 23 December 2013
Available online 31 December 2013

*Keywords:*
Mesoporous titania films
Pt doping
Stearic acid degradation
Methylene Blue photobleaching
Hydroxyl radical production

ABSTRACT

The preparation, characterization, and photoactivity of mesoporous Pt-$TiO_2$ thin films were investigated. Titania based thin films were prepared by evaporation induced self assembly (EISA) process, Pt being introduced by a non-photochemical process via two different ways. Whatever the synthesis method and the Pt content (between 0.5% and 3%), the prepared films were thin (around 200 nm) and mesoporous with an average pore size of 5 nm. XPS surface analysis showed that Pt was present in different oxidation states: mainly $Pt^0$ but also $Pt^{2+}$ and $Pt^{4+}$. The presence of $Pt^0$ nanoparticles was also clearly evidenced by Transmission Electronic Microscopy. The photocatalytic efficiency of the mesoporous titania films was determined by two different tests under both UV and visible light: the reaction rates and photonic efficiencies were determined for the mineralization of stearic acid (SA) at the gas–solid interface and for the solid–liquid photobleaching of Methylene Blue (MB). In all the cases, Pt-doped titania films were less active than pure $TiO_2$ films under UV light and slightly more active under visible light. Preliminary results on the $HO^\bullet$ production on the surface of the films were obtained from the reaction of a specific probe (terephtalic acid, TA) in basic aqueous solutions. These results were discussed relative to literature data.


## 1. Introduction

Titanium dioxide is a well-known photocatalyst, widely used in air or water treatment through mineralization of organic compounds under UV light [1,2] for its anti-fogging [3] and self-cleaning properties [4], as well as for its applications in solar energy conversion [5]. In order to achieve the high surface area and large porosity needed for high efficiency, numerous studies have also been devoted to the synthesis of mesoporous $TiO_2$ [6]. Highly organized and crystallized mesoporous $TiO_2$ films appear very promising to achieve a high photocatalytic activity under UV light for water [7–9] and air purification [10], for self-cleaning applications [11] and for photoelectrochemical conversion [12]. To extend $TiO_2$ absorption range to the visible light region, doping titania with metal ions may be used to promote the formation of electronic states within the gap between the conduction and the valence bands [1,5].

Photocatalytic properties of the extensively studied Pt-doped $TiO_2$ were reported to vary considerably depending on various parameters such as the nature of the substrate to be transformed on one hand, and on the other hand on the morphology, mass, particle size [13], dispersion [14], and oxidation state of Pt [15], these latter parameters being controlled by Pt doping method, mainly photodeposition or chemical deposition [16].

Platinum metal ($Pt^0$) modified $TiO_2$, synthesized by photodeposition of $Pt^{IV}$ salts, is well known to enhance photocatalytic activity under UV light because of the fast transfer of photogenerated electron from the conduction band of $TiO_2$ to Pt particles resulting in an efficient charge separation [17] and to a decrease of electron–hole pair recombination [18,19]. $Pt^0$ doped $TiO_2$ presented high photocatalytic activity for degradation of various substrates, such as CO [20], chlorinated organic compounds [21], methanol [22], toluene [23], benzyl alcohol (under visible light [24]). On the contrary, Siemon et al. found that platinized P25 had a decreased activity for EDTA decomposition in water [16].

Visible-light activated Pt-$TiO_2$ could be obtained by chemical deposition with chloroplatinic acid during the sol–gel synthesis of $TiO_2$: under these synthetic conditions, $Pt^{IV}$ and $Pt^{II}$ oxidation states were prevailing over $Pt^0$ [15]. For instance, Kim et al. [15] and Yamazaki [25] reported that $Pt^{4+}$-$TiO_2$ obtained by sol–gel method was as active as $Pt^0$-$TiO_2$ for the degradation of dichloroacetate and 4-chlorophenol under UV light, but more active under visible light. Visible and UV-light induced oxidation rates of aqueous Methylene Blue, iodide and phenol were shown to be enhanced for $Pt^{II}/Pt^{IV}$-doped $TiO_2$ relative to bare $TiO_2$ and was also correlated with the rutile ratio in doped titania samples [26]. Some papers were devoted to gas-phase visible light photocatalytic reactions. Adding

* Corresponding author. Tel.: +33 559 574 487.
*E-mail addresses:* thierry.pigot@univ-pau.fr (T. Pigot), sylvie.lacombe@univ-pau.fr (S. Lacombe).

0926-3373/$ – see front matter © 2014 Elsevier B.V. All rights reserved.
http://dx.doi.org/10.1016/j.apcatb.2013.12.042

of $PtO_x$ on $TiO_2$ promoted the visible-light photocatalytic oxidation of NO to $NO_2$ and $NO_3^-$ under blue, green and red LED irradiation [27]. Acetaldehyde degradation under UV and visible light was shown to increase with Pt-doping and to depend on calcination temperature of rutile $TiO_2$ [28]. A detailed Electron Spin Resonance (ESR) and chemiluminescence study concluded that the visible light irradiation (>500 nm) of a commercial $PtCl/TiO_2$, representative of "sensitized" photocatalysts, led to the charge separation into $Pt^{3+}$ and Cl radicals: visible light Interfacial Charge Transfer (IFCT) to produce valence band holes would be involved in the reaction mechanism [29]. From the recent study of Choi team [14], the morphology of mesoporous Pt-$TiO_2$ strongly influences the cluster size and dispersion of Pt together with the photocatalytic activity.

Mesoporous $TiO_2$ with large surface area, uniform pore size and open frameworks for mass transfer has already many applications in photocatalysis [6–11]. Recently Ismail et al. reported the preparation of mesoporous $Pt^0$-$TiO_2$ nanocomposites with the highest measured photonic efficiency for methanol oxidation [30] and for hydrogen production [31] under UV light, attributed to bi-crystalline framework, large surface area and high crystallinity. Mesoporous $Pt^0$-$TiO_2$ multilayers thin films were more active for acetaldehyde oxidation under UV light than commercial dense photocatalytic glasses. The deposited Pt particles enhanced the photonic efficiency by two times whatever the number of layers by acting as trapping centers for photo-generated electrons [32,33].

In the present study, mesoporous anatase $TiO_2$ based films were prepared by dip-coating via two EISA processes. The influence of the synthetic method and of the doping level on the structure and photocatalytic properties was investigated. The films were fully characterized by XRD, TEM, DRUV and X-ray Photoelectron Spectroscopy. The photocatalytic efficiency of the mesoporous titania films was determined by two different tests under both UV and visible light: solid–solid degradation of stearic acid and solid–liquid degradation of Methylene Blue. Preliminary results on the $OH^\bullet$ production were obtained from the reaction of a specific probe (terephthalic acid) in basic aqueous solutions.

## 2. Experimental

$TiCl_4$, $PtCl_4$, non-ionic surfactant F127, terephthalic acid and stearic acid were purchased from Sigma–Aldrich. Spectroscopic grades absolute ethanol (EtOH) and chloroform were purchased from Merck.

### 2.1. Synthesis of titania based films

$TiO_2$ films were synthesized according to a previously reported method from transparent and homogenous solution containing $TiCl_4$/EtOH/$H_2O$/F127 with a molar ratio of 1/40/10/0.005 [34]. $TiCl_4$ was added to EtOH and $H_2O$ before addition of F127. This solution was stirred for 30 min. Pure and doped films were deposited on either silicium wafer or glass plates at 2.8 cm $s^{-1}$ by EISA. During deposition, a low humidity (15%) is needed to induce fast evaporation of solvents leading to formation of micelles and formation of hybrid mesophase. After deposition, films were let at high humidity (85% for 24 h) to stabilize the network, before thermal treatment at 350 °C for 3 h to remove the template and heating at 550 °C for 10 min to obtain crystallized anatase$TiO_2$ based films.

Pt-$TiO_2$ films were elaborated by two different ways:

(a) Route 1: the dopant was added with others precursors during the synthesis.
(b) Route 2: the $TiO_2$ suspension was made first as mentioned before then, after stirring for 30 min, the Pt dopant was added prior deposition. Four $PtCl_4$ contents (0.005; 0.01; 0.02; 0.03 mol relative to $TiCl_4$) were used for preparation of *x*Pt-$TiO_2$ (1) and *x*Pt-$TiO_2$ (2) for route 1 and 2 respectively where x is atomic percentage of Pt ($x$ = 0.5, 1, 2, 3).

### 2.2. Characterization of the films

X-ray diffraction (XRD) measurements were performed on a D8 Bruker apparatus operating at the Cu Kalpha1 radiation ($\lambda$ = 1.5406 Å). Transmission Electronic Microscopy (TEM) pictures were obtained with a Philips CM 200 (200 kV) instrument equipped with a $LaB_6$ source. The samples dispersed in ethanol were dropped onto a carbon copper grid and dried before analysis. Films thickness and refractive index were determined using variable angle spectroscopic ellipsometer (VASE) from Woolam. The data analysis was performed with WVase32 software. Environmental Ellipsometric Porosimetry (EEP) device was commercialized by SOPRA Co. EEP data were analyzed by SOPRA software. The diffuse reflectance (DRUV) spectra of the samples were measured with a Perkin-Elmer 860 Spectrophotometer equipped with a 15 cm diameter integrating sphere bearing the sample holder in the bottom horizontal position. The surface atomic composition and chemical environment were analyzed by X-ray photoelectron spectra (XPS) measurements on a Thermo K-alpha system with a hemispherical analyzer and a microfocussed (analysis area was ca. 200 $\mu m^2$) monochromatized radiation Al K$\alpha$ line (1486.6 eV) operating at 75 W under a residual pressure of $1 \times 10^{-7}$ mBar. The spectrometer pass energy was set to 200 eV for survey spectrum and to 20 eV for core peak records. Surface charging was minimized using a neutralizer gun, which sprays the low energy electrons and $Ar^+$ ions over the sample surface. All the binding energies were calibrated with the C 1s peak at 285.0 eV originating from the surface contamination carbon. The treatment of core peaks was carried out using a nonlinear Shirley-type background [35]. A weighted least-squares fitting method using 70% Gaussian, 30% Lorentzian line shapes was applied to optimize the peak positions and areas. The quantification of surface composition was based on Scofield's relative sensitivity factors [36].

### 2.3. Photocatalytic tests

#### 2.3.1. Photo-decomposition of stearic acid (SA) and monitoring by FTIR

The experimental procedure was derived from Mill's published work [37]. 100 µl of a $10^{-2}$ M SA solution in chloroform was deposited on films by spin coating (spinning at 500 rpm $s^{-1}$ for 3 min and accelerating at 1000 rpm $s^{-1}$ for 10 s). After drying, the films were then irradiated with four fluorescent tubes (Philips TL 8 W for UV lamps centered on 365 nm, light intensity 3.5 mW $cm^{-2}$, or Rayonet RPR4190Å visible lamps with a 420 nm cutoff filter (Schott), light intensity 11 mW $cm^{-2}$, see Figs S1 and S2-SI for lamps emission spectra. Light intensities were measured with a spectro-radiometer (International Light Technologies ILT900) periodically calibrated. The degradation of SA was followed by FTIR spectroscopy by integrating the signal related to the stretching bands of C—H bonds of SA between 2800 and 3000 $cm^{-1}$.

#### 2.3.2. Photo-decomposition of stearic acid (SA) and monitoring by ellipsometry

Using the same variable angle spectroscopic ellipsometer (VASE) for thickness and refractive index, the ellipsometric parameters can be measured dynamically under UV LED irradiation. In this work, SA photocatalytic degradation was monitored by following the variation of the refractive index with time. SA was deposited by infiltrating the pores with a SA solution in chloroform in order to completely fill the pores. The samples were then placed in a well-closed cell with a control of humidity at a distance of 5 cm from

the 250 mW Nichia NCSU033A 365 nm UV-light emitting diode (LED). UV-light intensity was 40 mW $cm^{-2}$. Preliminary tests indicated that the photocatalytic activity was the highest at 50% relative humidity which was used for all the following experiments.

#### 2.3.3. Photo-decomposition of Methylene Blue (MB)

The photobleaching of MB, commonly used to monitor the photocatalytic activity of various media, was recently normalized via ISO 10678 (2010) [38]. The experimental procedure was adapted from Mills et al. [37,39] by directly irradiating a film in the UV–vis spectrometer. The film was located on the backside of a fluorescence cuvette perpendicular to the monitoring UV–vis beam. Before starting any experiment, a pre-adsorption of a MB solution in water on Titania films (initial MB concentration $2 \times 10^{-5}$ M) for 12 h in the dark was achieved. Then, a solution of MB ($10^{-5}$ M) containing a Titania film was irradiated with a LED (light power 8 mW $cm^{-2}$ in both cases) at 365 or 420 nm (see irradiance spectra in Fig S2-SI). The rate of MB photobleaching was determined from MB absorbance at 665 nm.

#### 2.3.4. Determination of hydroxyl radicals produced in aqueous solution

3 mL of a $5 \times 10^{-4}$ M terephthalic acid (TA) solution in $2 \times 10^{-3}$ M aqueous NaOH in a fluorescence cuvette containing a Titania based film (same geometry as previously) was irradiated with the previously used 365 nm LED. The fluorescence of 2-HTA was then recorded with time and 2-HTA concentration was deduced from the fluorescence curve established in a previous step with pure synthesized 2-HTA [40].

## 3. Results and discussions

### 3.1. Synthesis of films

Titania based thin films were prepared by EISA process [34]. Controlling humidity during the sol–gel synthesis is a critical factor for obtaining the desired film structure [41]. The thickness of the synthesized films were determined by ellipsometry and ranged between 200 and 180 (± 20) nm respectively for $TiO_2$ and Pt-$TiO_2$. Refractive index measured at 700 nm for pure $TiO_2$ was 1.65 and an increase was observed to 1.7 when Pt content increased.

### 3.2. X-Ray diffraction analysis

XRD results revealed only anatase phase for both $TiO_2$ and Pt-$TiO_2$ thin films (diffractograms in Fig. S3-SI). No platinum species was detected in the XRD patterns for the Pt-$TiO_2$ films owing to the small Pt content. It may be concluded that Pt did not affect the microstructure of Titania, in agreement with Kim et al. [15] In addition, the crystallite diameter was calculated from the full width at half maximum (FWHM) of diffraction peaks by using the Debye–Scherrer formula: the average crystallite size of titania based films calcined at 550 °C is evaluated to 7.5 nm.

### 3.3. Porosimetry and TEM characterization

Mesostructuration was demonstrated by Transmission Electronic Microscopy (TEM) and Environmental Ellipsometric Porosimetry (EEP). As shown in Fig. 1a, TEM images of non-doped $TiO_2$ presented a grid-like structure, achieved by diffuse sintering of nanocrystallites of $TiO_2$ in agreement with a previous study [34]. From Fig. 1b, two features were observed for Pt-$TiO_2$ whatever the Pt content or the synthetic method: first, the mesostructure was maintained and second, the presence of well dispersed Pt particles with sizes between 2.5 and 3 nm was evidenced.

EEP was used to determine pores volume (from the water adsorption–desorption isotherms) [42] and size. Isotherms represent the volume percent of water adsorbed versus relative pressure of water for selected titania thin films with different Pt concentrations prepared via route 1 (Fig. 2a). All isotherms have a typical behavior of mesoporous materials. The maximal measured porosity was 40%, corresponding to non-doped titania, while pores volume varied between 35% and 40% for Pt-$TiO_2$. Pore size distribution of pure $TiO_2$ and Pt-$TiO_2$ were centered at 4.5 and 5 nm in diameter respectively (Fig. 2b). Our results indicate that Pt doping did not modify significantly the mesoporosity of Pt-$TiO_2$ (1) films while porous volume decrease significantly for the highest Pt content of Pt-$TiO_2$ (2).

### 3.4. UV–vis reflectance spectra

Pure $TiO_2$ exhibited the absorption edge around 380 nm corresponding to the typical band gap of anatase $TiO_2$ (Fig. 3). In comparison to pure $TiO_2$ and in agreement with previous data [14], the absorption was extended to higher wavelength when 0.5–3% Pt was added for both Pt-$TiO_2$ (1) and Pt-$TiO_2$ (2), with a more significant shift for Pt-$TiO_2$ (1). These results are consistent with mixed spectra assigned to both Localized Surface Plasmon resonance of $Pt^0$ nanoparticles and ionic platinum $Pt^{2+}$ and $Pt^{4+}$ [15], as confirmed by the following XPS data.

### 3.5. X-ray photoelectron spectroscopy

The doped $TiO_2$ samples were investigated by X-ray photoelectron spectroscopy in order to study the electronic structure and the Pt content on the catalysts surface. The C*1s*, O*1s*, Ti*2p* and Pt*4f* spectra were recorded for all the samples in order to check the influence of the doping on the surface atoms. The presence of carbon is due to the surface carbon contamination. The analyses were performed twice to ensure the homogeneous dispersion of Pt on the surface of the samples.

The Pt doping did not affect the Ti*2p* and O*1s* core peaks for all the samples. The ionic character of the O—Ti bond remains unchanged by the platinum substitution since the difference between the $O_{1s}$ and $Ti_{2p}$ bond energy value is around 71.3 eV for all the samples. Fig. 4 presents the typical Pt*4f* core peaks of the doped Pt-$TiO_2$ (1) and Pt-$TiO_2$ (2) samples. They revealed two main components Pt $4f_{7/2}$ and Pt $4f_{5/2}$ due to the spin orbit coupling. The Pt spectra always revealed three oxidation states of platinum after doping whatever the synthesis route. Based on literature data, the Pt $4f_{7/2}$ peaks located at 73.6 eV, 71.8 eV and 70.8 eV were attributed, respectively, to $Pt^{4+}$, $Pt^{2+}$ and/or $Pt(OH)_2$ and $Pt^0$ [43,44]. The Pt*4f* core peaks exhibit the same characteristic whatever the Pt content.

Different evolution of atomic ratios can be observed depending on the synthesis route (Table 1). The $O_I$/Ti ratio is less than two for all samples with a higher deviation from the stoichiometry for the route 1 samples. For these samples, the Pt/Ti ratios revealed the expected increase of the Pt content with a slight deviation from the nominal one, while the hydroxyl groups content ($O_{II}$/Ti) also clearly increased with the Pt content. The $Pt^{2+}$ proportion was roughly constant, whereas a continuous decrease of the $Pt^{4+}$/Pt ratio and increase of the $Pt^0$/Pt was noticed with the increase of the total Pt amount. The formation of $Pt^0$ can be explained by the acidic pH of the initial solution ($pH \leq 0$). According to the literature, changing the preparation conditions can control Pt oxidation state: Pt oxides were deposited under alkaline conditions whereas $Pt^0$ was mainly deposited under acidic pH [45]. The evolution of each atomic ratio did not follow a clear evolution for the samples synthesized by route 2.

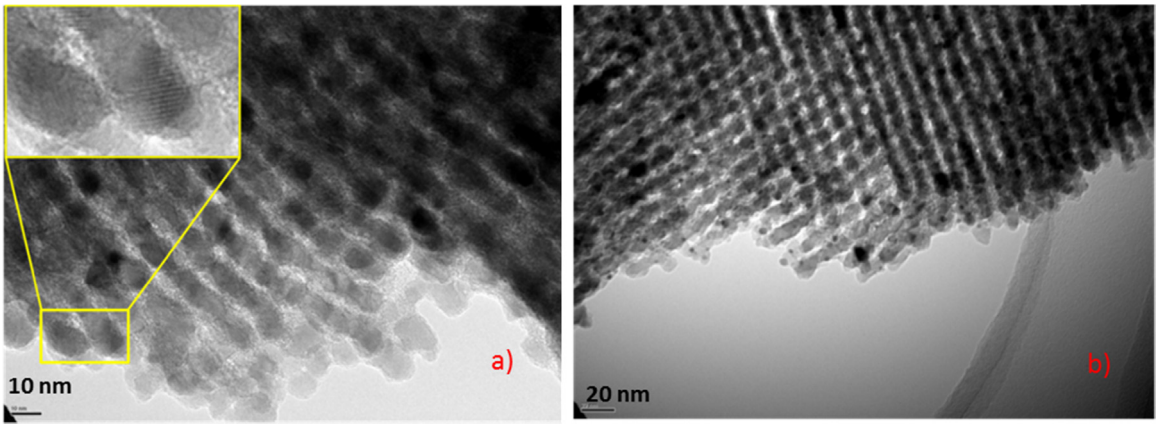


**Fig. 1.** TEM images of (a) pure $TiO_2$ (b) 3 Pt-$TiO_2$ (1).

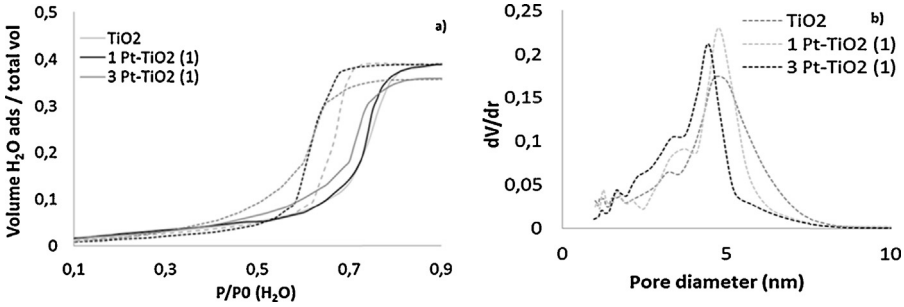


**Fig. 2.** (a) Adsorption (solid line) – desorption (dotted line) isotherms plotted for $TiO_2$ and *x*Pt-$TiO_2$ (1) with different Pt contents; (b) pore size distributions deduced from the desorption curves.

### 3.6. Photocatalytic properties

SA is commonly used to determine self-cleaning properties, although, to the best of our knowledge, no studies dealing with its photodegradation on Pt-doped $TiO_2$ was previously reported. The photocatalytic activity of $TiO_2$-based films was followed by the disappearance of SA characteristic IR bands under UV and visible light. First, control experiments showed no SA degradation without $TiO_2$ under UV or visible light. As shown in Fig. S4-SI and as expected from literature data [37], SA absorbance decreased with increasing UV irradiation time. Ollis developed different simple kinetic models for the photocatalysed removal of SA films [46]. Depending on the photocatalyst-film configuration, the degradation rate followed a zero order kinetic law (when SA films overlayed on photocatalyst) or a first-order law (when SA was present within the pores of the photocatalyst). In our case, the degradation of SA on pure Titania was found to follow a pseudo-first-order kinetic law as shown in the inserts (Fig. 5b and d). Photonic efficiencies $\Phi_E$ (Fig. 5a and c) were determined as the ratio of the photo-reaction rate (defined as the number of SA degraded molecules $s^{-1}$ $cm^{-2}$ deduced from the IRTF data) to the incident light intensity in photons $s^{-1}$ $cm^{-2}$ (Calculation details in Section S5-SI). Under UV light, the photonic efficiency $\Phi_E$ or formal quantum efficiency [37] decreased with the increase of Pt content for both Pt-$TiO_2$ (1) and Pt-$TiO_2$ (2), with a slightly greater effect for Pt-$TiO_2$ (2) (Fig. 5a). It can be concluded that pure $TiO_2$ film showed the highest activity and that platinum had detrimental effect on photocatalytic SA decomposition.

Using the same variable angle spectroscopic ellipsometer (VASE) for thickness and refractive index, the ellipsometric parameters can be measured dynamically under UV LED irradiation. Monitoring the change of both thickness and refractive index with the UV irradiation time can correlate the photocatalytic activity of the films. This method was already used to characterize the change in optical parameters of the films with time by Remillard et al.

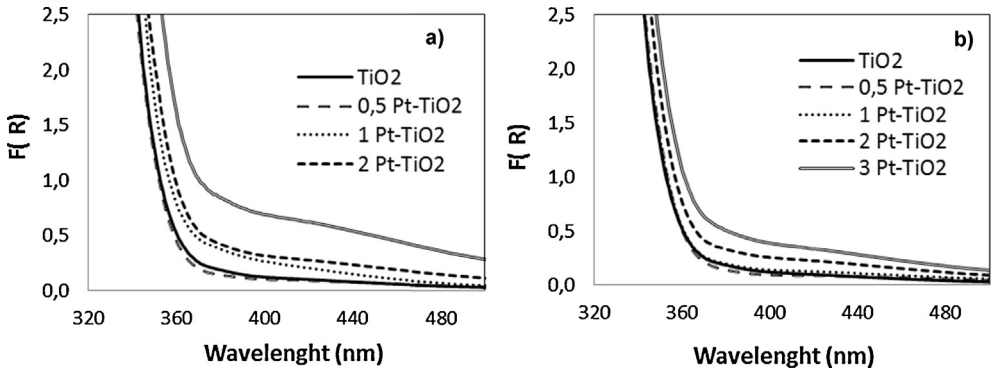


**Fig. 3.** UV–vis diffuse reflectance spectra for (a) Pt-$TiO_2$ (1) and (b) Pt-$TiO_2$ (2).

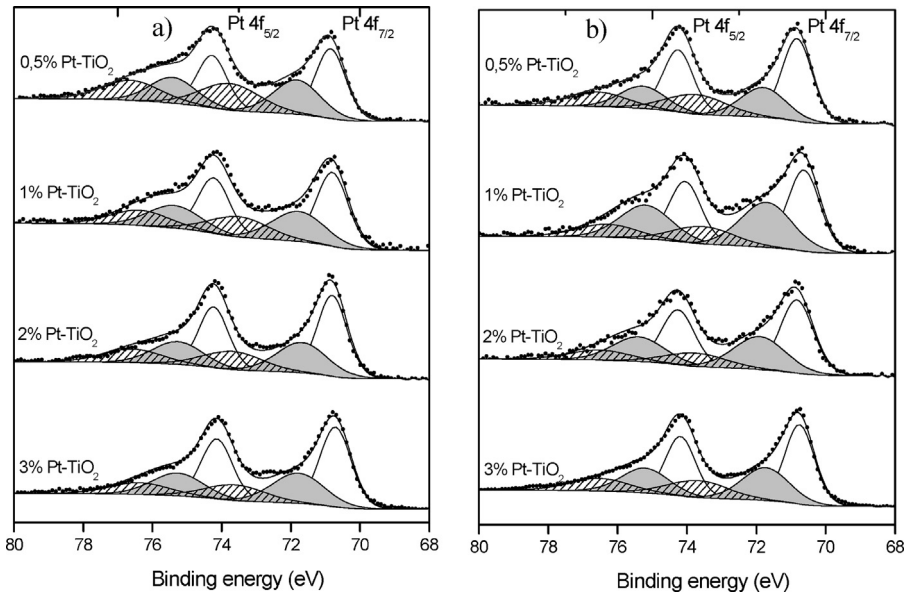


**Fig. 4.** XPS $Pt^{4f}$ core peaks of (a): Pt-$TiO_2$ (1) and (b): Pt-$TiO_2$ (2). White peaks are assigned to $Pt^0$, *t* gray peaks to $Pt^{2+}$, and hatched peaks to $Pt^{4+}$.

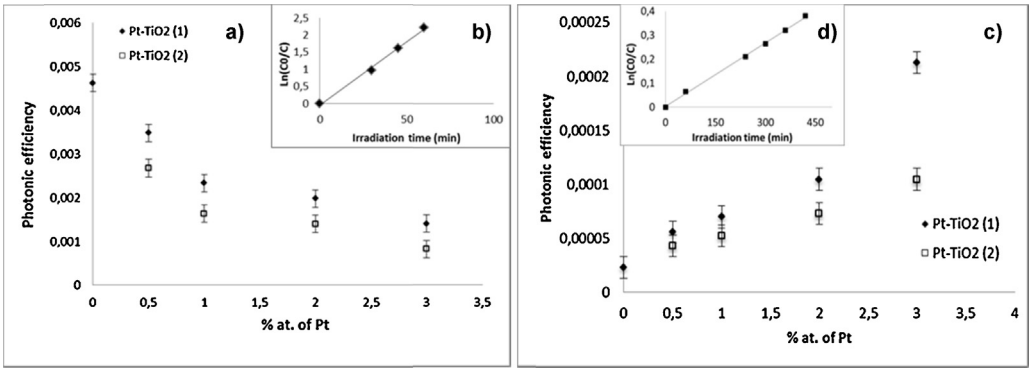


**Fig. 5.** Photonic efficiencies of SA degradation versus Pt content (a) under UV and (c) visible light. Inserts: $\ln(C_0/C)$ of SA degradation versus time (b) on $TiO_2$ film under UV light and (d) on 3 Pt-$TiO_2$ (1) under visible light.

[49]. Recently, Carretero-Genevrier et al. studied the local photocatalytic activity at the surface of $TiO_2$ films using ellipsometry [50]. The decreased reaction rates with increasing Pt content were thus also confirmed monitoring of SA decomposition under 365 nm LED irradiation (40 mW $cm^{-2}$): the refractive index decreased from 1.9 which corresponds to pores filled with SA to 1.65 corresponding to completely open pores, while $TiO_2$ thickness remained constant (Fig. 6).

Under visible irradiation, a different trend was observed, since the photonic efficiency increased with Pt content (Fig. 5c), although the calculated values were much weaker ($2.3 \times 10^{-5}$–$2.0 \times 10^{-4}$) than under UV light ($8 \times 10^{-4}$–$4.6 \times 10^{-3}$). These values are significantly greater than the values obtained by Mills et al. on dense Pillkinton Activ TM and $TiO_2$ P25 films respectively ($1.53 \times 10^{-4}$ and $7 \times 10^{-6}$) at 365 nm. According to these authors, the maximum $\Phi_E$ value is $9.6 \times 10^{-3}$ if the 104 electrons needed for SA complete oxidation are taken into account. This means that our values under UV light are closer to these theoretical one, due to our much higher conversion factor between the IR integrated absorbance and the number of molecules $cm^{-2}$ (1 $cm^{-1}$ corresponds to $10^{17}$ molecules SA $cm^{-2}$ versus $9.7 \times 10^{15}$ molecules SA $cm^{-2}$ in [37], see Fig. 6-SI). This result may be assigned to the fact that our film are much thicker

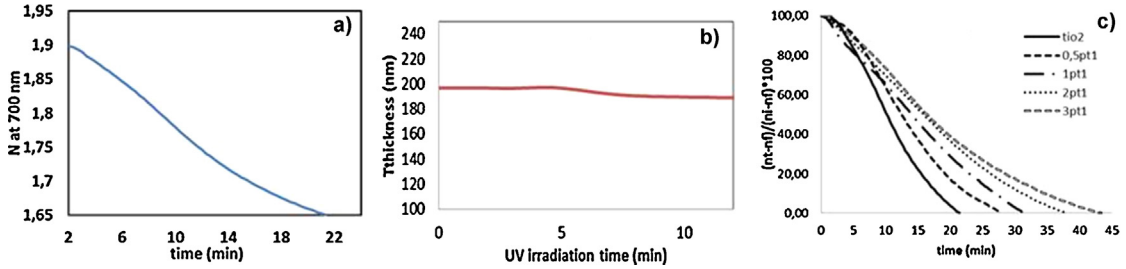


**Fig. 6.** (a) Variation of refractive index of pure titania film upon UV irradiation at 365 nm; (b) variation of thickness of pure titania film upon UV irradiation at 365 nm; (c) effect of Pt content on variation of SA quantity upon irradiation at 365 nm.

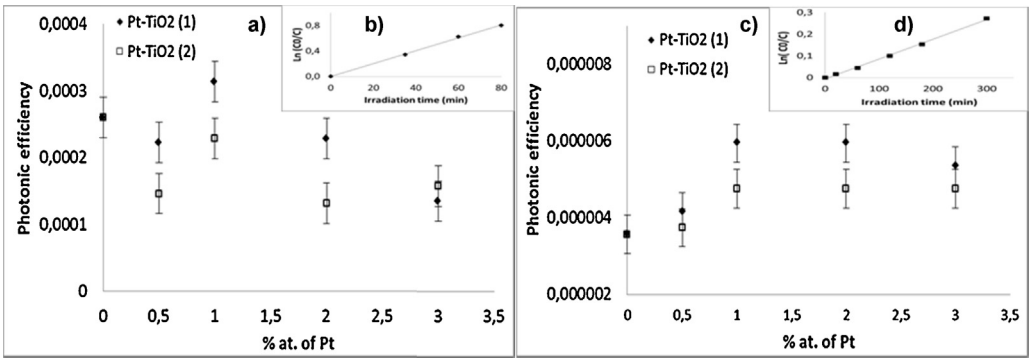


**Fig. 7.** Photonic efficiencies of MB photobleaching versus Pt content (a) under UV and (c) visible light. Inserts: $\ln(C_0/C)$ of MB photobleaching versus time (b) on $TiO_2$ film under UV light and (d) on 3 Pt-$TiO_2$ (1) under visible light.

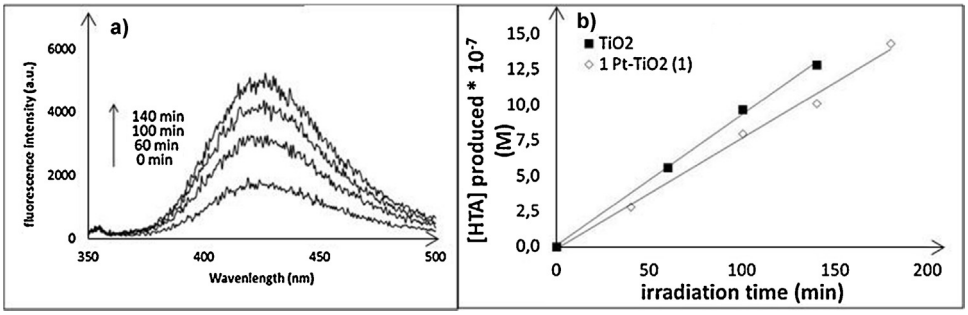


**Fig. 8.** (a) Emission spectra of HTA with UV irradiation time from terephtalate aqueous solution containing pure $TiO_2$ and 1 Pt-$TiO_2$ (1) (b) [HTA] with UV irradiation time from terephtalate aqueous solution containing pure $TiO_2$ and 1 Pt-$TiO_2$ (1) films.

**Table 1**
Atomic ratio of Pt-$TiO_2$ (1) and (2) films from XPS spectra.

| | Pt-$TiO_2$ (1) | | | | |
|---|---|---|---|---|---|
| | $TiO_2$ | 0.5% Pt | 1% Pt | 2% Pt | 3% Pt |
| $O_{Oxyde}/Ti$ | 1.91 | 1.86 | 1.83 | 1.78 | 1.78 |
| $O_{ads}/Ti$ | | 0.25 | 0.48 | 0.43 | 0.90 |
| Pt/Ti | | 0.02 | 0.02 | 0.04 | 0.07 |
| $Pt^0/Pt$ | | 0.40 | 0.44 | 0.48 | 0.52 |
| $Pt^{2+}/Pt$ | | 0.30 | 0.31 | 0.31 | 0.30 |
| $Pt^{4+}/Pt$ | | 0.30 | 0.25 | 0.21 | 0.19 |
| | Pt-$TiO_2$ (2) | | | | |
| | 0.5% Pt | | 1% Pt | 2% Pt | 3% Pt |
| $O_{Oxyde}/Ti$ | 1.82 | | 1.90 | 1.90 | 1.81 |
| $O_{ads}/Ti$ | 0.46 | | 0.41 | 0.30 | 0.33 |
| Pt/Ti | 0.03 | | 0.05 | 0.06 | 0.04 |
| $Pt^0/Pt$ | 0.51 | | 0.40 | 0.47 | 0.48 |
| $Pt^{2+}/Pt$ | 0.27 | | 0.36 | 0.36 | 0.31 |
| $Pt^{4+}/Pt$ | 0.22 | | 0.44 | 0.36 | 0.21 |

and porous relative to dense films, and that stearic acid is first filling the 40% volume void pores in agreement with our first order kinetic constant of the 180–200 nm thick films as stated by Ollis [46]. This also implies a very high activity of the mesoporous films relative to dense ones as already observed by Allain et al. [11] and reported by Tschirch et al. ($\Phi_E$: 4.3–5.9 × $10^{-3}$ for 200 and 400 nm thick mesoporous films respectively) [8].

The negative or positive effect of Pt on the efficiency of $TiO_2$ was extensively discussed in the literature [14]. However, to our knowledge, our results provide the first evidence of different behavior under UV or visible light for stearic acid decomposition, with an optimum 3% Pt concentration for maximum visible efficiency, in line with previous data (0.5–2% Pt atom.) [26]. Our results also demonstrate that films prepared by route 1 are generally more active than those prepared by route 2, particularly under visible light. At last, the first order kinetic results obtained for these mesoporous films are fully consistent with Ollis's model of SA inside the pores.

MB photobleaching in the presence of the mesoporous films (Fig. S7-SI) also followed a first order kinetic law (Fig. 7b and d). The calculated first order kinetic constants and photonic efficiency $\Phi_E$ (see Table 2-SI for detailed calculations) were about tenfold lower both under UV and visible light than for SA degradation and much less sensitive to the Pt content. Under UV and visible light, a maximum efficiency was observed for 1 Pt-$TiO_2$ with a non-significant difference between films prepared by route 1 or 2 (Fig. 7a and c).

To further investigate the relative photocatalytic efficiency of the Pt-$TiO_2$ films, we used terephatalate in basic aqueous solutions as a selective probe of HO• formation [47]. For undoped $TiO_2$ and 1-Pt-$TiO_2$ (1), we observed the characteristic fluorescence of hydroxyteterephtalate (HTA) showing the formation of HO• on the surface of the films under UV-A irradiation (Fig. 8a). The concentration of HTA increased linearly with time (Fig. 8b). Since the concentration of 2-HTA was proportional to the amount of produced HO•, we deduced that the production of HO• followed a pseudo-zero order kinetic law.

The formation rate of HO• on $TiO_2$ thin film was estimated to $2 \times 10^{-8}$ M min$^{-1}$ when the formation rate on 1 Pt-$TiO_2$ (1) was slightly lower ($1.67 \times 10^{-8}$ M min$^{-1}$). The photonic efficiency for the HO• radicals for pure $TiO_2$ was evaluated to $2.7 \times 10^{-5}$ for and to $2.2 \times 10^{-5}$ for 1 Pt-$TiO_2$ (1). These values are slightly lower but of the same order of magnitude than those published by Fujishima et al. [48], and a slight negative effect of Pt on HO• production is evidenced from these data. Pt obviously does not favor HO•

production and this is correlated with a decrease of activity under UV against stearic acid decomposition. Under visible light, it was shown that stearic acid decomposition was one order of magnitude slower than under UV and, in our conditions, $HO^{\bullet}$ was under the level of detection.

Our results confirm the complexity of the relevant parameters accounting for the negative effect of Pt observed in some cases and highlight different reactivity between UV and visible light. As mentioned before, in our case, $Pt^0$ represented 50% of total Pt while the other 50% were attributed to $Pt_{ox}$ composed of $Pt^{2+}$ and $Pt^{4+}$. The former has a favored role in inhibiting recombination of electron/hole pairs [17], while the latter can have a detrimental effect and acts as recombination center [15]. Thus, in our case, a competition between these two effects could modulate the photocatalytic activity.

## 4. Conclusion

This work describes the synthesis by EISA process, the characterization and the photocatalytic properties of undoped and Pt-doped titania thin films. The results suggested that the same microstructure and mesostructure was obtained for Pt-$TiO_2$ films whatever the doping route used. For both synthetic methods, well-dispersed Pt particles were obtained with a homogeneous size of 2–3 nm. As expected from the chemical Pt deposition process, the major Pt species was found to be $Pt^0$ (50%), together with oxidized Pt species ($Pt^{2+}$ and $Pt^{4+}$).

Photocatalytic activity of the films was compared either for solid SA decomposition or for MB photobleaching in aqueous solution. In all cases, Pt doping has a detrimental effect on UV-A photocatalytic properties of the films while a slight enhancement of photoactivity was observed under visible light. The photoactivity with UV light was correlated to the hydroxyl radical production and fewer radicals were produced on Pt-doped films surface. One reason of this decreased activity could be the presence on the surface of oxidized platinum favoring recombination processes. Further investigations on surface reactivity and direct identification by fluorescence microscopy of reactive species on the surface of the films are currently in progress.

## Acknowledgment

Agence Nationale pour la Recherche (ANR) is gratefully acknowledged for funding this work (project MEPHISTO ANR-10-BLAN-0803).

## Appendix A. Supplementary data

Supplementary data associated with this article can be found, in the online version, at http://dx.doi.org/10.1016/j.apcatb.2013.12.042.

## References

[1] A. Fujishima, X. Zhang, D.A. Tryk, Surf. Sci. Rep. 63 (2008) 515–582.
[2] S. Malato, P. Fernández-Ibáñez, M.I. Maldonado, J. Blanco, W. Gernjak, Catal. Today 147 (2009) 1–59.
[3] F.Ç. Cebeci, Z. Wu, L. Zhai, R.E. Cohen, M.F. Rubner, Langmuir 22 (2006) 2856–2862.
[4] A. Mills, S.-K. Lee, J. Photochem. Photobiol. A: Chem. 152 (2002) 233–247.
[5] S.G. Kumar, L.G. Devi, J. Phys. Chem. A 115 (2011) 13211–13241.
[6] R. Zhang, A.A. Elzatahry, S.S. Al-Deyab, D. Zhao, Nano Today 7 (2012) 344–366.
[7] J. Rathouský, V. Kalousek, M. Kolář, J. Jirkovský, Photochem. Photobiol. Sci. 10 (2011) 419–424.
[8] J. Tschirch, D. Bahnemann, M. Wark, J. Rathouský, J. Photochem. Photobiol. A: Chem. 194 (2008) 181–188.
[9] J.H. Pan, Z. Lei, W.I. Lee, Z. Xiong, Q. Wang, X.S. Zhao, Catal. Sci. Technol. 2 (2011) 147–155.
[10] V. Kalousek, J. Tschirch, D. Bahnemann, J. Rathouský, Superlattices Microstruct. 44 (2008) 506–513.
[11] E. Allain, S. Besson, C. Durand, M. Moreau, T. Gacoin, J.-P. Boilot, Adv. Funct. Mater. 17 (2007) 549–554.
[12] D. Feng, W. Luo, J. Zhang, M. Xu, R. Zhang, H. Wu, et al., J. Mater. Chem. A 1 (2013) 1591–1599.
[13] J.J. Murcia, J.A. Navío, M.C. Hidalgo, Appl. Catal. B: Environ. 126 (2012) 76–85.
[14] N. Lakshminarasimhan, A.D. Bokare, W. Choi, J. Phys. Chem. C 116 (2012) 17531–17539.
[15] S. Kim, S.-J. Hwang, W. Choi, J. Phys. Chem. B 109 (2005) 24260–24267.
[16] U. Siemon, D. Bahnemann, J.J. Testa, D. Rodríguez, M.I. Litter, N. Bruno, J. Photochem. Photobiol. A: Chem. 148 (2002) 247–255.
[17] M. Anpo, M. Takeuchi, J. Catal. 216 (2003) 505–516.
[18] H. Uetsuka, C. Pang, A. Sasahara, H. Onishi, Langmuir 21 (2005) 11802–11805.
[19] A. Yamakata, T. Ishibashi, H. Onishi, J. Phys. Chem. B 105 (2001) 7258–7262.
[20] S. Hwang, M.C. Lee, W. Choi, Appl. Catal. B: Environ. 46 (2003) 49–63.
[21] J. Lee, W. Choi, J. Phys. Chem. B 109 (2005) 7399–7406.
[22] C. Wang, R. Pagel, D.W. Bahnemann, J.K. Dohrmann, J. Phys. Chem. B 108 (2004) 14082–14092.
[23] G. Colón, M. Maicu, M.C. Hidalgo, J.A. Navío, A. Kubacka, M. Fernández-García, J. Mol. Catal. A: Chem. 320 (2010) 14–18.
[24] Y. Shiraishi, D. Tsukamoto, Y. Sugano, A. Shiro, S. Ichikawa, S. Tanaka, et al., ACS Catal. 2 (2012) 1984–1992.
[25] S. Yamazaki, Y. Fujiwara, S. Yabuno, K. Adachi, K. Honda, Appl. Catal. B: Environ. 121–122 (2012) 148–153.
[26] J. Choi, H. Park, M.R. Hoffmann, J. Phys. Chem. C 114 (2010) 783–792.
[27] C.-H. Huang, I.-K. Wang, Y.-M. Lin, Y.-H. Tseng, C.-M. Lu, J. Mol. Catal. A: Chem. 316 (2010) 163–170.
[28] Y. Ishibai, J. Sato, T. Nishikawa, S. Miyagishi, Appl. Catal. B: Environ. 79 (2008) 117–121.
[29] M. Nishikawa, H. Sakamoto, Y. Nosaka, J. Phys. Chem. A 116 (2012) 9674– 9679.
[30] A.A. Ismail, D.W. Bahnemann, Green Chem. 13 (2011) 428–435.
[31] T.A. Kandiel, A.A. Ismail, D.W. Bahnemann, Phys. Chem. Chem. Phys. 13 (2011) 20155–20161.
[32] A.A. Ismail, D.W. Bahnemann, Chem. Eng. J. 203 (2012) 174–181.
[33] A.A. Ismail, D.W. Bahnemann, J. Rathousky, V. Yarovyi, M. Wark, J. Mater. Chem. 21 (2011) 7802–7810.
[34] Y. Sakatani, D. Grosso, L. Nicole, C. Boissière, G.J. de, A.A. Soler-Illia, C. Sanchez, J. Mater. Chem. 16 (2006) 77–82.
[35] D.A. Shirley, Phys. Rev. B 5 (1972) 4709–4714.
[36] J.H. Scofield, J. Electron Spectrosc. Relat. Phenom. 8 (1976) 129–137.
[37] A. Mills, J. Wang, J. Photochem. Photobiol. A: Chem. 182 (2006) 181–186.
[38] ISO, Geneva, ISO 10678, 2010.
[39] A. Mills, A. Lepre, N. Elliott, S. Bhopal, I.P. Parkin, S.A. O'Neill, J. Photochem. Photobiol. A: Chem. 160 (2003) 213–224.
[40] E.B. Yan, J.K. Unthank, M. Castillo-Melendez, S.L. Miller, S.J. Langford, D.W. Walker, J. Appl. Physiol. 98 (2005) 2304–2310.
[41] E.L. Crepaldi, G.J. de, A.A. Soler-Illia, D. Grosso, F. Cagnol, F. Ribot, C. Sanchez, J. Am. Chem. Soc. 125 (2003) 9770–9786.
[42] C. Boissiere, D. Grosso, S. Lepoutre, L. Nicole, A.B. Bruneau, C. Sanchez, Langmuir 21 (2005) 12362–12371.
[43] M. Peuckert, H.P. Bonzel, Surf. Sci. 145 (1984) 239–259.
[44] A.S. Karakoti, J.E.S. King, A. Vincent, S. Seal, Appl. Catal. A: Gen. 388 (2010) 262–271.
[45] F. Zhang, J. Chen, X. Zhang, W. Gao, R. Jin, N. Guan, et al., Langmuir 20 (2004) 9329–9334.
[46] D. Ollis, Appl. Catal. B: Environ. 99 (2010) 478–484.
[47] S.E. Page, W.A. Arnold, K. McNeill, J. Environ. Monit. 12 (2010) 1658–1665.
[48] K. Ishibashi, A. Fujishima, T. Watanabe, K. Hashimoto, J. Photochem. Photobiol. A: Chem. 134 (2000) 139–142.
[49] J.T. Remillard, J.R. McBride, K.E. Nietering, A.R. Drews, X. Zhang, J. Phys. Chem. B 104 (2000) 4440–4447.
[50] A. Carretero-Genevrier, C. Boissiere, L. Nicole, D. Grosso, J. Am. Chem. Soc. 134 (2012) 10761–10764.